Multi-User Pre-Processing in Multi-Antenna OFDM TDD Systems with Non-Reciprocal Transceivers

Mark Petermann, Markus Stefer, Frank Ludwig, Dirk Wübben, *Senior Member, IEEE*, Martin Schneider, Steffen Paul, *Member, IEEE*, and Karl-Dirk Kammeyer, *Member, IEEE*

***Abstract*—The combination of OFDM with joint pre-processing in adaptive multi-antenna systems offers both an ease of equalization in frequency-selective channels and keeping the signal processing at the mobile stations simple. In addition, the spatial dimension can be efficiently exploited to ensure high system throughput. With the utilization of higher-order modulation the performance of the system is highly sensitive to multiple access interference and nonorthogonal subchannels due to hardware impairments or insufficient adaptation to the current channel conditions. A further source of error in TDD systems are the non-reciprocal transceivers inhibiting the baseband-to-baseband channel reciprocity required for accurate channel state acquisition based on the uplink channel estimate. In this paper, measurement results of a low-cost hardware-based calibration are presented and the drawbacks are discussed leading to the utilization of a recently introduced relative calibration. The latter is applied to an OFDM system and achieves or at least approximates the baseband-to-baseband reciprocity. Thus, it enables the link adaptation using the uplink channel state information. Furthermore, preliminary hardware implementations of the relative calibration running on a real-time system show accurate results.**

***Index Terms*—TDD, OFDM, reciprocity, impairments, calibration.**

I. Introduction

THE ability to adapt to the instantaneous downlink (DL) channel is crucial to achieve ever increasing data rates. The adaptation ability relies on the downlink channel availability at the base station (BS). The DL channel state information (CSI) has to be fed back by the mobile subscriber (MS) to the base station in case of a frequency-division-duplex (FDD) system. This results in a huge overhead in the uplink (UL). To reduce the latter significantly, it is reasonable to exploit the reciprocity theorem [1]. Consequently, this means exchanging the FDD system for a time-division-duplex (TDD) system. The theorem holds as long as the coherence time of the physical channel is large compared to the time of the duplex phase. A decisive problem arises in that the reciprocity of the system is lost when considering baseband-to-baseband transmission because of the non-symmetric characteristics of the analog transmit (Tx) and receive (Rx) frontends. Furthermore, non-linearities within the devices inhibit a reciprocal behavior. In [2], [3], this objective is described in detail as well as the deterioration of the system performance in absence of the reciprocity due to hardware impairments. In addition, receiver-side algorithms are introduced in [2], [3] to compensate for the hardware effects. Alternative solutions exist to compensate or even avoid the effects leading to non-reciprocal communication systems. Firstly, the transceiver is dimensioned such that the identical hardware is used for the transmit and receive path [4]. Secondly, another method aims at calibrating the transmitter and receiver arrays separately using additional hardware. The latter helps to identify the differences of the individual frontend characteristics and the compensation is realized with respect to a reference antenna [5]. If adaptation to the DL is pursued utilizing the uplink channel state information, it is judicious to additionally execute a (pre-)equalization with respect to space and adapt the modulation scheme and the power allocation per subcarrier in an Orthogonal-Frequency-Division-Multiplexing (OFDM) system. The requirements regarding the quality of the available CSI at the BS increase especially with respect to choosing the maximum feasible modulation scheme.

So far it can be concluded that the CSI available at the BS has to be of high quality to fulfill the aforementioned demands. Conversely, the utilization of the UL-CSI at the base station in a TDD system shows a poor quality as a consequence of the violation of the reciprocity theorem considering baseband-to-baseband communication. The hardware-based concepts are costly and do not allow an online calibration. The signal-processing-based concepts in [2], [3] use receiver-side compensation algorithms.

We pursue a different concept in that a low-complexity hardware-based concept and a signal-processing-based concept both allowing for online calibration are investigated.

The outline of the paper is as follows. First, the system model used to reflect these effects within the communication system is explained in Section II and is grounded on scattering parameters describing the different transceiver blocks and the antennas. Based on this system model, we verify the suggested concept of [6] in Section III that provides the opportunity of a relative calibration of the base station. In [6],

Manuscript received December 21, 2012; revised April 19, 2013. The editor coordinating the review of this paper and approving it for publication was M. Juntti.

This work was supported in part by the German Research Foundation (DFG) under grant KA841-21/2, PA438-3/2 and SCHN1147-2/2.

M. Petermann, D. Wübben, and K.-D. Kammeyer are with the Department of Communications Engineering, University of Bremen, Germany (e-mail: {petermann, wuebben, kammeyer}@ant.uni-bremen.de).

M. Stefer and M. Schneider are with the RF & Microwave Engineering Laboratory, University of Bremen, Germany (e-mail: {markus.stefer, martin.schneider}@hf.uni-bremen.de).

F. Ludwig and S. Paul are with the Department of Communication Electronics, University of Bremen, Germany (e-mail: {ludwig, steffen.paul}@me.uni-bremen.de).

Digital Object Identifier 10.1109/TCOMM.2013.072813.120984

a low-cost hardware-based concept is proposed including the respective calibration procedure. The main advantages over the former hardware-based concepts are the low costs and the ability to perform an online calibration. With respect to a full calibration - this would involve the base station and the mobile subscribers - the drawbacks are also discussed. To be able to avoid the deployment of additional hardware it has to be accepted that the reciprocity will not be fulfilled. As a consequence, the goal has to be to compensate for the effects conditioned by the hardware by means of signal processing techniques [7]. In [8]–[11], a relative calibration procedure is presented that is feasible for MIMO-single-carrier systems (Multiple-Input Multiple-Output). The procedure is discussed in detail in Section IV-A, where it is transfered to a joint multi-user (MU) MISO-OFDM system (Multiple-Input Single-Output). Results based on simulations are presented and discussed comparing systems with uncoupled antennas to systems with mutually coupled antennas. These results show the technique to be feasible in terms of practically relevant influences.

Since the concept is proven to be feasible, Section IV-B discusses the possibility of implementing the relative calibration on a system running in real-time, e.g., FPGA (Field Programmable Gate Array). The main challenge here is to efficiently realize the singular value decomposition (SVD) on an FPGA. To assess the performance, comparisons are drawn to existent realizations regarding the needed execution time. Section V concludes the paper by evaluating the results.

Throughout this paper, $(\cdot)^T$ denotes the transpose, $(\cdot)^H$ the conjugate transpose, $(\cdot)^*$ the complex conjugate, $\mathrm{tr}\{\cdot\}$ the trace of a matrix, $(\cdot)^{-1}$ the inverse and the Moore-Penrose pseudoinverse is denoted by $(\cdot)^\dagger$. The vec-operator $\mathrm{vec}\{\cdot\}$ is defined as the operator stacking the columns of a matrix and $\otimes$ denotes the Kronecker product. The $\mathrm{diag}\{\cdot\}$ operator maps a vector onto the diagonal elements of a matrix, while $\mathrm{diag}^{-1}\{\cdot\}$ maps the diagonal elements of a matrix onto a vector. Boldface capital letters denote matrices, boldface lower-case letters denote vectors and lower-case letters denote scalars.

II. System Model

In this section, an appropriate system model is introduced that combines the system equation in communications with the scattering parameter description established in high-frequency technology. Section II-A presents the considered communication scenario and Section II-B describes the scattering parameter modeling of the hardware. Section II-C delves into the specific effect of mutual coupling between antenna elements and Section II-D concretizes the generally introduced hardware effects and states the chosen simulation parameters. Concluding remarks about multi-user induced interference in high signal-to-interference plus noise regions and the resultant calibration idea are given in Section II-E.

A. Multi-User Joint Signal Pre-Processing in OFDM Systems

In the following, a downlink scenario consisting of a base station equipped with $N_{\mathcal{B}}$ antennas and $N_{\mathcal{M}}$ decentralized and non-cooperative single-antenna mobile stations is considered.

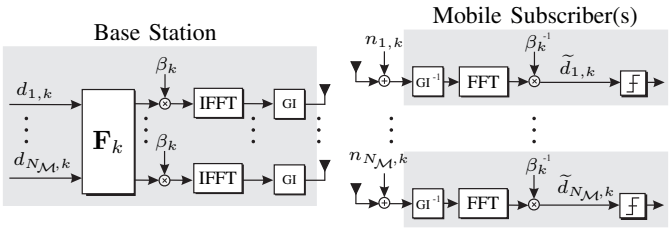

Fig. 1. Block diagram of the considered multi-user MISO-OFDM system with joint pre-processing in the frequency-domain.

As the exploitation of TDD channel reciprocity is limited by the physical channel reciprocity depending on channel coherence time, an office environment with non-moving receivers is assumed throughout the paper. In addition, in such an office scenario high signal-to-noise ratios can be expected and high data rates are usually requested (cf. Section II-E). Fig. 1 shows the block diagram of the multi-user MISO-OFDM system consisting of N_{sc} subcarriers with joint pre-processing in the frequency-domain. The vector of transmit symbols per antenna in time-domain is obtained by pre-processing the M-QAM symbol vector $\mathbf{d}_k = [d_{1,k}, \ldots, d_{i,k}, \ldots, d_{N_{\mathcal{M}},k}]^T$ with variance $\mathbf{I}_{N_{\mathcal{M}}}$ applying the linear pre-equalization matrix $\mathbf{F}_k$ per subcarrier k. To satisfy a total power constraint of $N_{\mathcal{B}}$ per OFDM symbol at the BS, the transmit symbols per subcarrier k are multiplied with a common scalar β_k. The application of the Inverse Fast Fourier Transform (IFFT) yields the time-domain signals, which are extended by adding a guard interval (GI). In case of a sufficiently long guard time the channel impulse response is fully contained in the GI and inter-symbol interference (ISI) is avoided. Furthermore, a cyclic convolution of the OFDM symbol with the mobile radio channel is achieved. As a consequence of ISI avoidance, the system equation can be simplified to a matrix-vector multiplication per subcarrier k. At the mobile stations, complex Gaussian i.i.d. noise samples with variance σ_{n}^2 are added to describe the noise influence. At the single-antenna mobile stations, the GI is removed, followed by the transformation into frequency-domain by applying the Fast Fourier Transform (FFT). The processing is completed by dividing the received signal by β_k with respect to every subcarrier k. The system equation corresponding to Fig. 1 reads

$$\tilde{\mathbf{d}}_k = \mathbf{H}_k \mathbf{F}_k \mathbf{d}_k + \beta_k^{-1} \mathbf{n}_k \,, \tag{1}$$

where the receive signal vector $\tilde{\mathbf{d}}_k$ contains the data of the mobile subscribers and the downlink channel matrix is denoted by $\mathbf{H}_k$. The filter matrix $\mathbf{F}_k$ is given by $\mathbf{F}_k^{(\mathrm{ZF})} = \mathbf{G}_k^\dagger$ in case of Zero-Forcing (ZF) or $\mathbf{F}_k^{(\mathrm{MMSE})} = \mathbf{G}_k^H (\mathbf{G}_k \mathbf{G}_k^H + N_{\mathcal{M}}\, \sigma_{\mathrm{n}}^2 \mathbf{I}_{N_{\mathcal{B}}})^{-1}$ in case of minimum mean square error (MMSE) linear pre-equalization. Here, the matrix $\mathbf{G}_k$ denotes the transposed uplink channel matrix. The scalar

$$\beta_k = \sqrt{\frac{N_{\mathcal{B}}}{\mathrm{tr}\left\{\mathbf{F}_k^H \mathbf{F}_k\right\}}} \tag{2}$$

is chosen such that the total sum power constraint per subcarrier k is fulfilled.

The UL- and DL-CSI available at the BS has to be estimated and is therefore inaccurate in general. The present errors due

to channel estimation can be factored in by an MMSE channel predictor model like in [12] or, as it is rendered here, by modeling the Least Squares (LS) estimate $\hat{\mathbf{G}}_k$ of the actual channel matrix $\mathbf{G}_k$ in terms of the MSE with the use of a correlation factor ϱ_e. Instead of performing channel estimation, the estimated UL channel matrix $\hat{\mathbf{G}}_k$ of one subcarrier k can then be modeled by

$$\hat{\mathbf{G}}_k = \varrho_\mathrm{e}\,\mathbf{G}_k + \sqrt{\varrho_\mathrm{e}\,(1-\varrho_\mathrm{e})}\,\mathbf{\Psi}_k\,, \tag{3}$$

where $\mathbf{\Psi}_k$ is a Gaussian error matrix with zero mean and entry variance of one and $\sigma_\mathrm{e}^2 = 1-\varrho_\mathrm{e}^2$ is a normalized estimation error power restricted to the interval $\sigma_\mathrm{e}^2 \in [0,1]$. For simulation purposes, this error power is assumed equal on all subcarriers and ensures that the power of one estimate is equal to the power of the corresponding true channel. In contrast, correlation between subcarriers, which usually occurs when applying LS or MMSE estimation in combination with interpolation in pilot-based schemes, is neglected. However, this simple model is sufficient to summarize estimation errors for further analyses.

B. Radio-frequency-based Baseband Model

To quantify the influence of non-ideal transceiver hardware on the effective baseband channels, an appropriate scattering matrix model based on microwave network theory exists in the literature [13], [14].

This model is illustrated here in detail to give a comprehensive overview with the focus on how to incorporate the respective hardware effects appropriately.

Fig. 2 shows a block diagram illustrating the communication model by means of scattering parameter blocks at a fixed frequency k. The physical downlink channel is denoted by $\mathbf{S}_{\mathcal{MB},k} \in \mathbb{C}^{N_\mathcal{M}\times N_\mathcal{B}}$ and the physical uplink channel by $\mathbf{S}_{\mathcal{BM},k} \in \mathbb{C}^{N_\mathcal{B}\times N_\mathcal{M}}$. The mutual coupling between the different antenna elements is denoted by $\mathbf{S}_{\mathcal{BB},k} \in \mathbb{C}^{N_\mathcal{B}\times N_\mathcal{B}}$ regarding the base station and denoted by $\mathbf{S}_{\mathcal{MM},k} \in \mathbb{C}^{N_\mathcal{M}\times N_\mathcal{M}}$ regarding the mobile stations. Although the mobile subscribers are assumed to be equipped with a single antenna, the system model is derived with respect to the more general case of mobile subscribers with multiple antennas. With respect to the downlink in the analog baseband, the transmit signal of the base station is denoted by $\widetilde{\mathbf{a}}_{\mathcal{B},k}$ and the receive signals at the mobile stations by $\widetilde{\mathbf{b}}_{\mathcal{M},k}$. Correspondingly in the uplink, the transmit signals of the mobile stations are described by $\widetilde{\mathbf{a}}_{\mathcal{M},k}$ and the receive signals at the base station by $\widetilde{\mathbf{b}}_{\mathcal{B},k}$. The goal now is to establish the relationship $\widetilde{\mathbf{b}}_{\mathcal{M},k} = \mathbf{S}_{\text{total,DL},k}\widetilde{\mathbf{a}}_{\mathcal{B},k}$ in the downlink, where $\mathbf{S}_{\text{total,DL},k}$ expresses the transmission characteristics between the base station and mobile stations. First of all, the scattering parameter description of the transceivers is introduced. The respective transmission characteristics are then translated into separate diagonal matrices. Only then it is possible to determine $\mathbf{S}_{\text{total,DL},k}$. The transmit and receive antenna frontends are characterized by two-port devices defined by the matrix

$$\mathbf{T}_{\mathcal{B},i,k} = \begin{bmatrix} 0 & 0 \\ \alpha_{\mathrm{T},\mathcal{B},i,k} & \gamma_{\mathrm{T},\mathcal{B},i,k} \end{bmatrix} \tag{4}$$

denoting the transmitter $i = 1,\ldots,N_\mathcal{B}$ of the base station and the matrix

$$\mathbf{R}_{\mathcal{M},j,k} = \begin{bmatrix} 0 & \alpha_{\mathrm{R},\mathcal{M},j,k} \\ 0 & \gamma_{\mathrm{R},\mathcal{M},j,k} \end{bmatrix} \tag{5}$$

denoting the receiver of mobile subscriber $j = 1,\ldots,N_\mathcal{M}$. The matrices $\mathbf{T}_{\mathcal{B},i,k}$ and $\mathbf{R}_{\mathcal{M},j,k}$ consist of complex conversion gain factors $\alpha_{\mathrm{T},\mathcal{B},i,k}$ and $\alpha_{\mathrm{R},\mathcal{M},j,k}$, as well as input reflection coefficients $\gamma_{\mathrm{T},\mathcal{B},i,k}$ and $\gamma_{\mathrm{R},\mathcal{M},j,k}$. The complex gain factors $\alpha_{\mathrm{T},\mathcal{B},i,k}$ and $\alpha_{\mathrm{R},\mathcal{M},j,k}$ and the reflection coefficients $\gamma_{\mathrm{T},\mathcal{B},i,k}$ and $\gamma_{\mathrm{R},\mathcal{M},j,k}$ are now arranged in diagonal matrices. Regarding the transmitters at the base station, the diagonal matrices are given by

$$\mathbf{A}_{\mathrm{T}\mathcal{B},k} = \mathrm{diag}\{\alpha_{\mathrm{T}\mathcal{B},1,k},\ldots,\alpha_{\mathrm{T}\mathcal{B},N_\mathcal{B},k}\} \tag{6a}$$

$$\mathbf{\Gamma}_{\mathrm{T}\mathcal{B},k} = \mathrm{diag}\{\gamma_{\mathrm{T}\mathcal{B},1,k},\ldots,\gamma_{\mathrm{T}\mathcal{B},N_\mathcal{B},k}\}\,, \tag{6b}$$

and the receivers of the mobile stations are assembled into

$$\mathbf{A}_{\mathrm{R}\mathcal{M},k} = \mathrm{diag}\{\alpha_{\mathrm{R}\mathcal{M},1,k},\ldots,\alpha_{\mathrm{R}\mathcal{M},N_\mathcal{M},k}\} \tag{7a}$$

$$\mathbf{\Gamma}_{\mathrm{R}\mathcal{M},k} = \mathrm{diag}\{\gamma_{\mathrm{R}\mathcal{M},1,k},\ldots,\gamma_{\mathrm{R}\mathcal{M},N_\mathcal{M},k}\}\,. \tag{7b}$$

Hence, exploiting (6) the analog baseband-to-baseband downlink channel is derived to obtain

$$\mathbf{S}_{\text{total,DL},k} = \mathbf{A}_{\mathrm{R}\mathcal{M},k}\mathbf{W}_{\mathrm{R}\mathcal{M},k}^T \mathbf{S}_{\mathcal{MB},k}\mathbf{W}_{\mathrm{T}\mathcal{B},k}\mathbf{A}_{\mathrm{T}\mathcal{B},k}\,. \tag{8}$$

The coupling matrices defined by

$$\mathbf{W}_{\mathrm{T}\mathcal{B},k} = (\mathbf{I}_{N_\mathcal{B}} - \mathbf{\Gamma}_{\mathrm{T}\mathcal{B},k}\mathbf{S}_{\mathcal{BB},k})^{-1} \tag{9a}$$

$$\mathbf{W}_{\mathrm{R}\mathcal{M},k} = (\mathbf{I}_{N_\mathcal{M}} - \mathbf{\Gamma}_{\mathrm{R}\mathcal{M},k}\mathbf{S}_{\mathcal{MM},k})^{-1} \tag{9b}$$

incorporate the influence of the reflection coefficients $\mathbf{\Gamma}_{\mathrm{T},\mathcal{B},k}$, $\mathbf{\Gamma}_{\mathrm{R},\mathcal{M},k}$ and the mutual coupling between antennas $\mathbf{S}_{\mathcal{BB},k}$, $\mathbf{S}_{\mathcal{MM},k}$ on the overall downlink channel $\mathbf{S}_{\text{total,DL},k}$. Translating (8) into the discretized domain regarding the subcarrier k finally yields

$$\mathbf{H}_k = \mathbf{A}_{\mathrm{R}\mathcal{M},k}\mathbf{W}_{\mathrm{R}\mathcal{M},k}^T\mathbf{S}_{\mathcal{MB},k}\mathbf{W}_{\mathrm{T}\mathcal{B},k}\mathbf{A}_{\mathrm{T}\mathcal{B},k}\,. \tag{10}$$

Replacing the index R by T and the index T by R in (10), a similar relation is obtained with respect to the matrix $\mathbf{G}_k$ denoting the transposed uplink channel matrix

$$\mathbf{G}_k = \mathbf{A}_{\mathrm{T}\mathcal{M},k}\mathbf{W}_{\mathrm{T}\mathcal{M},k}^T\mathbf{S}_{\mathcal{MB},k}\mathbf{W}_{\mathrm{R}\mathcal{B},k}\mathbf{A}_{\mathrm{R}\mathcal{B},k}\,. \tag{11}$$

Equation (11) already features the crucial modification exploiting the reciprocity theorem of the physical channel

$$\mathbf{S}_{\mathcal{MB},k} = \mathbf{S}_{\mathcal{BM},k}^T\,. \tag{12}$$

In conclusion, the total downlink scattering matrix (8) is directly linked with the downlink system equation (1) through (10). Regarding a more detailed derivation of the equations (4)-(11), the authors refer to [13] and [14].

C. Mutual Coupling Between Antennas

Since the antenna coupling in combination with the reflection coefficients of the transceivers influences the downlink and uplink channel, it justifies to take the antenna coupling into account. However, if antenna coupling is considered, heterogeneous interpretations exist [15]–[17]. In [16] and [17], the mutual coupling between isotropic radiators is introduced.

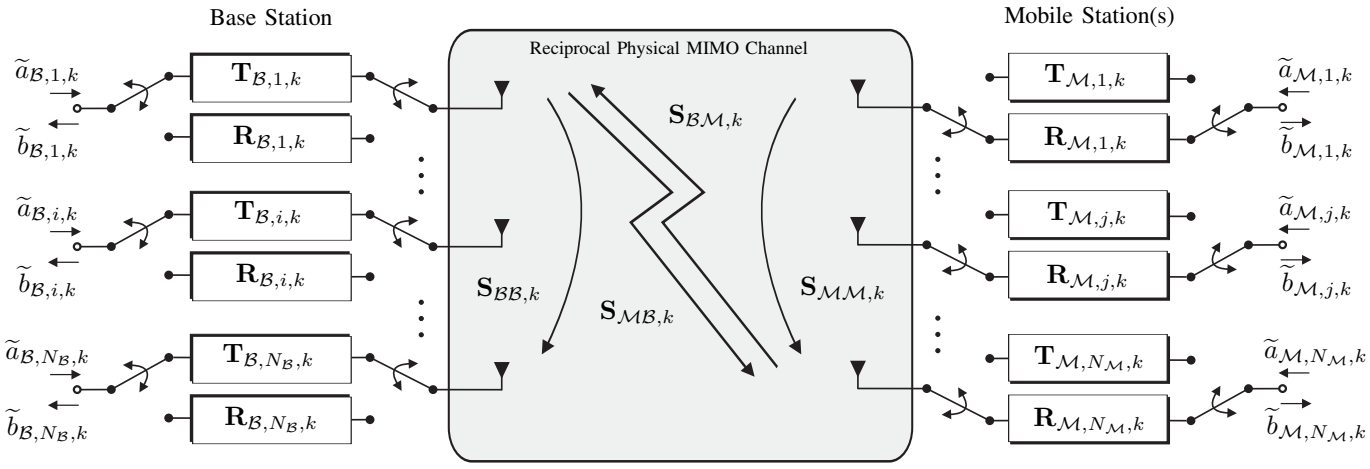

Fig. 2. Extended channel model using S-parameter description with BS and MS in downlink mode.

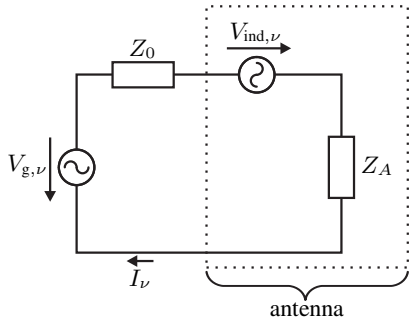

Fig. 3. Circuit theory motivated antenna model for one antenna element ν.

This might make sense in terms of a pure circuit theory point of view but from an antenna engineering point of view this would be related to the array factor [15]. Therefore, in addition to stating the mutual coupling in terms of the scattering matrix, the underlying physical context is also presented here.

If at least two antennas are placed closely to each other with respect to the wavelength and one of these antennas is driven by, e.g., a voltage source, the second antenna is irrevocably in the near-field of the driven and therefore transmitting antenna. Consequently, the transmitting antenna induces a voltage at the ports of the non-transmitting antenna, which is called mutual coupling. To obtain a measure for the mutual coupling, the induced voltage can be related to the impressed current on the transmitting antenna. The ratio between induced voltage and impressed current is called the mutual impedance. Here, the mutual impedance is examined to describe the mutual coupling between two antennas with indices ν and ξ. The mutual impedance $Z_{\xi\nu}$ according to circuit theory is defined as [15]

$$Z_{\xi\nu} = \frac{V_{\xi\nu}}{I_\nu} \ , \tag{13}$$

where $V_{\xi\nu}$ is the induced voltage at port ξ due to a current I_ν impressed at port ν [18]. Translating this to antenna theory, a circuit model for an antenna ν within an array of $N_\mathcal{B}$ elements can be established as is depicted in Fig. 3. The antenna is modeled by a series connection of its input impedance Z_A and an additional voltage source $V_{\text{ind},\nu}$. According to Fig. 3, the ideal generator voltage $V_{\text{g},\nu}$ with generator impedance Z_0 can be expressed as

$$V_{\text{g},\nu} = (Z_0 + Z_\text{A}) \cdot I_\nu + V_{\text{ind},\nu} \ . \tag{14}$$

The voltage $V_{\text{ind},\nu}$ is the induced voltage on antenna ν stemming from the current excitations of the remaining antenna elements $\xi = 1, \ldots, N_\mathcal{B} \, \forall \, \xi \neq \nu$, which is expressed by

$$V_{\text{ind},\nu} = \sum_{\xi=1,\xi\neq\nu}^{N_\mathcal{B}} Z_{\xi\nu} \, I_\xi \ . \tag{15}$$

Additionally, (15) makes use of the superposition principle for assembling the total induced voltage [18]. Rewriting the current and voltage relations indicated by (14) in matrix form, the impedance matrices $\mathbf{Z}_{\mathcal{B}\mathcal{B},k} \in \mathbb{C}^{N_\mathcal{B} \times N_\mathcal{B}}$ and $\mathbf{Z}_{\mathcal{M}\mathcal{M},k} \in \mathbb{C}^{N_\mathcal{M} \times N_\mathcal{M}}$ are obtained. With the calculated impedance matrices $\mathbf{Z}_{\mathcal{B}\mathcal{B},k}$ and $\mathbf{Z}_{\mathcal{M}\mathcal{M},k}$, the according scattering matrices $\mathbf{S}_{\mathcal{B}\mathcal{B},k}$ and $\mathbf{S}_{\mathcal{M}\mathcal{M},k}$ are obtained by employing [19]

$$\mathbf{S}_{\mathcal{B}\mathcal{B},k} = \left(\frac{\mathbf{Z}_{\mathcal{B}\mathcal{B},k}}{Z_0} + \mathbf{I}_{N_\mathcal{B}} \right)^{-1} \left(\frac{\mathbf{Z}_{\mathcal{B}\mathcal{B},k}}{Z_0} - \mathbf{I}_{N_\mathcal{B}} \right) \tag{16}$$

exemplary for the scattering matrix of base station. With respect to the antenna coupling between the mobile stations the scattering matrix $\mathbf{S}_{\mathcal{M}\mathcal{M},k}$ is obtained by replacing the index $\mathcal{B}$ in (16) with $\mathcal{M}$. Here, $Z_0 = 50 \ \Omega$ denotes the reference impedance of the antenna ports.

D. Modeling of the Individual System and Simulation Parameters

This section states the actual modeling and assumptions made regarding the different hardware components apparent in the downlink and the uplink.

- Ideally, the baseband-to-baseband transfer function resembles an allpass function. In reality however, this assumption cannot be preserved. Although the allpass characteristic of the baseband-to-baseband transfer function is not present, it is physically reasonable to model the transfer function to possess an *allpass-like* transfer function. The *allpass-like* behavior is implemented by adding a complex perturbation term to unity. This is

TABLE I
SIMULATION PARAMETERS USED THROUGHOUT THE PAPER.

Parameter	Symbol	Value
number of subcarriers	N_{sc}	256
guard interval length	N_g	6
coded modulation scheme	M	16-QAM
number of channel taps	L	6
punctured 3GPP Turbo Code	R_c	0.5
transmission scenario	$N_{\mathcal{M}} \times N_{\mathcal{B}}$	4×4

explained and applied in more detail in the following sub-item.

- The downlink involves the conversion gains of the transmitters at the base station $\alpha_{\text{T}\mathcal{B},i,k}$ and the conversion gains of the mobile stations $\alpha_{\text{R}\mathcal{M},i,k}$. According to the preceding sub-item, the conversion gains at the base station are modeled as $\alpha_{\text{T}\mathcal{B},i,k} = 1 + \delta_{\text{T}\mathcal{B},i,k}$ and $\alpha_{\text{R}\mathcal{B},i,k} = 1 + \delta_{\text{R}\mathcal{B},i,k}$ while setting the conversion gains of the mobile stations equal to one. The additional error terms $\delta_{\text{T}\mathcal{B},i,k}$ and $\delta_{\text{R}\mathcal{B},i,k}$ denote zero mean complex Gaussian random variables on each antenna i and subcarrier k. The variance of the error terms is assumed to be subcarrier-independent and identical for each antenna i, i.e., $\sigma^2_{\text{T}\mathcal{B}\delta,i,k}$ and $\sigma^2_{\text{R}\mathcal{B}\delta,i,k}$ simplify to σ^2_{δ}. It has to be pointed out that the behavior of the transceivers regarding this allpass-like transfer function behavior is feasible when considering relative bandwidths of $\approx 1\ \%$. The latter is maintained throughout this paper and is in accordance with the long-term-evolution (LTE) standardization [20].
- From an engineering point of view, it is reasonable to assume the mean value of the input reflection coefficients $\gamma_{\text{T}\mathcal{B},i,k}$ and $\gamma_{\text{R}\mathcal{B},i,k}$ to be equal to a typical value, in the following set to $-20\ \text{dB} \mathrel{\hat{=}} 0.1$ [21]. This results in the input reflection coefficient model $\gamma_{\text{T}\mathcal{B},i,k} = 0.1 + \kappa_{\text{T}\mathcal{B},i,k}$ and $\gamma_{\text{R}\mathcal{B},i,k} = 0.1 + \kappa_{\text{R}\mathcal{B},i,k}$, where $\kappa_{\text{T}\mathcal{B},i,k}$ and $\kappa_{\text{R}\mathcal{B},i,k}$ denote zero mean complex Gaussian random variables on each antenna i and subcarrier k. The error variance of the modeled input reflection coefficients is subcarrier-independent and identical for each transceiver i, i.e., $\sigma^2_{\text{T}\mathcal{B}\kappa,i,k}$ and $\sigma^2_{\text{R}\mathcal{B}\kappa,i,k}$ simplify to σ^2_{κ}.
- With respect to the base station, the antenna elements are considered to be "infinitesimally thin" $\lambda/2$ dipoles [22] and the input as well as the mutual impedance can be computed by using the results presented in [23]. Since the bandwidth of the baseband signal can be considered to be relatively small compared to the carrier frequency f, the impedances are presumed to be frequency-independent and are therefore only evaluated at the carrier frequency f. The impedance matrix $\mathbf{Z}_{\mathcal{B}\mathcal{B},k}$ as well as the according scattering matrix $\mathbf{S}_{\mathcal{B}\mathcal{B},k}$ simplify to $\mathbf{Z}_{\mathcal{B}\mathcal{B}}$ and $\mathbf{S}_{\mathcal{B}\mathcal{B}}$, respectively.
- From a physical point of view, it is legitimate to presume that no coupling is present between the single-antenna MS as the spacing between the users is at least of several wavelengths such that $\mathbf{S}_{\mathcal{M}\mathcal{M}}$ reduces to a scaled identity matrix $\mathbf{S}_{\mathcal{M}\mathcal{M}} = \frac{Z_{\text{A}}}{Z_{\text{A}}+2\,Z_0}\mathbf{I}_{N_{\mathcal{M}}}$.

If not otherwise stated, the simulation parameters summarized in Tab. I are used throughout the remaining sections.

E. Transceiver Impact and Calibration Objectives

The utilization of the UL channel matrix for pre-equalization in (1) leads to interference terms caused by the differences between (10) and (11). Thorough analytical treatments of the interference terms and the influence on the receive signal-to-interference plus noise ratios (SINR) for different types of pre-equalization are given in [14] and [24], [25]. The authors also provide some receive SINR analyses in [26]. All references commonly show that multi-user induced interference dominates the receive SINR deterioration in non-reciprocal systems especially if the users are in high transmit SNR regions, e.g., close to the base station. When being close to the base station high data rate processing is possible. In contrast, higher order modulations are more sensitive to interference effects.

These SINR considerations emphasize the contemplated indoor scenarios because of the influence of non-reciprocal transceivers at high transmit SNR regions. In the LTE context, these situations may occur more often when thinking about the femto-cell concept. To come full-circle, cheap low-power femto-cell MIMO base stations usually suffer even more from non-reciprocal transceiver characteristics substantiating the need for calibration. All calibration approaches pursue the suppression of multi-user or multi-antenna interference as the primal objective, which is the reason why similar methods do not apply in established single-antenna systems.

III. HARDWARE-BASED DOWNLINK CHANNEL CALIBRATION

The motivation for the hardware-based relative calibration is the compensation of the effects of different transmit and receive gains at the base station. Mathematically, the compensation can be accomplished by an additional diagonal calibration matrix $\mathbf{C}_k$ that is incorporated into the pre-equalization filter matrix, i.e., $\mathbf{F}_k = \mathbf{C}_k\mathbf{G}_k^{\dagger}$ in case of Zero-Forcing [6], [27]. Consequently, the compensation of the in general non-diagonal coupling matrices $\mathbf{W}_{\text{T}\mathcal{B},k}$ and $\mathbf{W}_{\text{R}\mathcal{M},k}$ cannot be accomplished and the approach is actually only reasonable when being able to neglect the mutual coupling. This is justified if the distance between antenna elements is around the half of a free-space wavelength in terms of the carrier frequency. Regarding this specific distance, the coupling can be assumed to be small and hence allows the assumption of $\mathbf{W}_{\text{T}\mathcal{B},k} \approx \mathbf{I}_{N_{\mathcal{B}}}$ and $\mathbf{W}^{-1}_{\text{R}\mathcal{M},k} \approx \mathbf{I}_{N_{\mathcal{M}}}$. In this case, the calibration matrix has to be designed such that

$$\underbrace{\mathbf{W}_{\text{T}\mathcal{B},k}}_{\approx\mathbf{I}_{N_{\mathcal{B}}}} \cdot \mathbf{A}_{\text{T}\,\mathcal{B},k} \cdot \mathbf{C}_k \cdot \mathbf{A}^{-1}_{\text{R}\,\mathcal{B},k} \cdot \underbrace{\mathbf{W}^{-1}_{\text{R}\mathcal{M},k}}_{\approx\mathbf{I}_{N_{\mathcal{M}}}} = \frac{\alpha_{\text{T}\mathcal{B},1,k}}{\alpha_{\text{R}\mathcal{B},1,k}} \cdot \mathbf{I} \quad (17)$$

is fulfilled. The remaining factor on the right hand side of (17) specifies transceiver 1 of the base station as the reference transceiver. Consequently, the described calibration approach illustrates a relative calibration. It has to be pointed out that this approach relies on an additional equalization at the mobile stations to at least compensate for $\alpha_{\text{T}\mathcal{B},1,k}/\alpha_{\text{R}\mathcal{B},1,k}$. The design regulation in (17) leads to the following values of

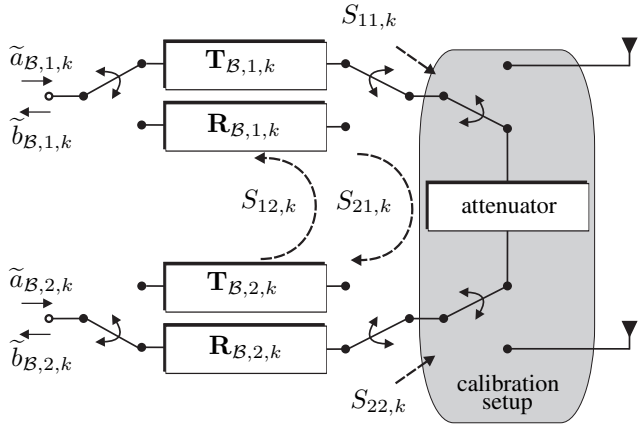

Fig. 4. Calibration setup attached to base station transceivers.

the calibration matrix $\mathbf{C}_k = \mathrm{diag}\{c_{1,k}, \ldots, c_{N_\mathcal{B},k}\}$

$$c_{1,k} = 1$$
$$c_{i,k} = \frac{\alpha_{\mathrm{T}\mathcal{B},1,k}}{\alpha_{\mathrm{R}\mathcal{B},1,k}} \frac{\alpha_{\mathrm{R}\mathcal{B},i,k}}{\alpha_{\mathrm{T}\mathcal{B},i,k}}. \tag{18}$$

The $c_{i,k}$ can be calculated using a calibration setup proposed by [6] resulting in an improvement in terms of a lower bit error rate (BER) without providing measurement results. In [27], simulation results are reported and discussed that prove this concept to be feasible. The additional hardware needed to realize the calibration consists of two single-pole-double-throw (SPDT) switches and an attenuator in case of a base station equipped with two transceivers. The MIMO demonstrator introduced in [28], [29] implements a base station with two transceivers and can be used to verify the concept with respect to measurement results. The attenuator is necessary to avoid overdriving the receive chains of the transceivers [6], [27] and is realized by a commercially available digital-step-attenuator to adjust for a good signal-to-noise ratio with respect to the calibration procedure.

1) Calibration Procedure: Fig. 4 schematically shows the base station with the attached calibration setup.

$$\widetilde{b}_{\mathcal{B},2,k} = \widetilde{S}_{21,k}\, \alpha_{\mathrm{T}\mathcal{B},1,k}\, \alpha_{\mathrm{R}\mathcal{B},2,k}\, \widetilde{a}_{\mathcal{B},1,k} + n_{21,k} \tag{19a}$$
$$\widetilde{S}_{21,k} = \frac{S_{21,k}}{1 + \gamma_{\mathrm{R}\mathcal{B},2,k}(S_{21,k}\, S_{12,k} - S_{22,k} + \gamma_{\mathrm{T}\mathcal{B},1,k}\, S_{11,k}\, S_{22,k})} \tag{19b}$$
$$\widetilde{b}_{\mathcal{B},1,k} = \widetilde{S}_{12,k}\, \alpha_{\mathrm{T}\mathcal{B},2,k}\, \alpha_{\mathrm{R}\mathcal{B},1,k}\, \widetilde{a}_{\mathcal{B},2,k} + n_{12,k} \tag{19c}$$
$$\widetilde{S}_{12,k} = \frac{S_{12,k}}{1 + \gamma_{\mathrm{R}\mathcal{B},1,k}(S_{21,k}\, S_{12,k} - S_{11,k} + \gamma_{\mathrm{T}\mathcal{B},2,k}\, S_{11,k}\, S_{22,k})} \tag{19d}$$

By transmitting a pilot signal from the transmitter of transceiver 1 to the receiver of transceiver 2, (19a) contains the gain factors $\alpha_{\mathrm{T}\mathcal{B},1,k}$ and $\alpha_{\mathrm{R}\mathcal{B},2,k}$, the overall forward transmission coefficient $\widetilde{S}_{21,k}$ of the calibration setup and an additional noise term $n_{21,k}$ regarding each subcarrier k. Changing the direction of transmission, i.e., transmitting from transceiver 2 to transceiver 1 yields (19c) containing the gain factors $\alpha_{\mathrm{T}\mathcal{B},2,k}$ and $\alpha_{\mathrm{R}\mathcal{B},1,k}$, the overall reverse transmission coefficient $\widetilde{S}_{12,k}$ of the calibration setup and again an additional noise term $n_{12,k}$. The overall forward transmission coefficient $\widetilde{S}_{21,k}$ in (19b) and the overall backward transmission coefficient $\widetilde{S}_{12,k}$ in (19d) also contain the influences due to finite matching of the calibration setup, i.e., $S_{11,k} \neq 0$ and $S_{22,k} \neq 0$. Furthermore, the influence of imperfect transceiver matching is present in (19b) and (19d). Both effects, imperfect matching of the calibration setup as well as the imperfect matching of the transceivers deteriorate the calibration performance.

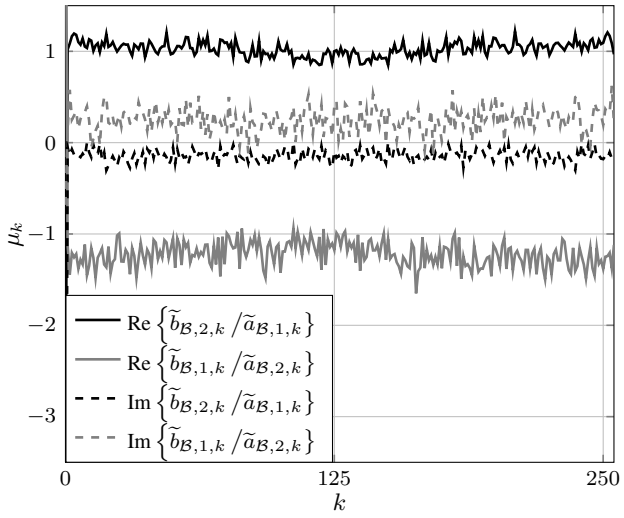

Fig. 5. Mean value μ_k of the base station's measured transfer functions of transmitter 1 to receiver 2 ($\widetilde{b}_{\mathcal{B},2,k}\,/\widetilde{a}_{\mathcal{B},1,k}$) and transmitter 2 to receiver 1 ($\widetilde{b}_{\mathcal{B},1,k}\,/\widetilde{a}_{\mathcal{B},2,k}$).

By taking several measurements according to (19a) and (19c), the noise can be averaged out to obtain the calibration parameter $c_{2,k}$

$$c_{2,k} = \frac{\widetilde{b}_{\mathcal{B},2,k}}{\widetilde{a}_{\mathcal{B},1,k}} \frac{\widetilde{a}_{\mathcal{B},2,k}}{\widetilde{b}_{\mathcal{B},1,k}}$$
$$= \frac{\alpha_{\mathrm{T}\mathcal{B},1,k}}{\alpha_{\mathrm{R}\mathcal{B},1,k}} \frac{\alpha_{\mathrm{R}\mathcal{B},2,k}}{\alpha_{\mathrm{T}\mathcal{B},2,k}} \frac{\widetilde{S}_{21,k}}{\widetilde{S}_{12,k}}. \tag{20}$$

The only difference between (20) and (18) is the ratio $\widetilde{S}_{21,k}/\widetilde{S}_{12,k}$ of the forward and reverse transmission coefficients of the calibration setup. The desired value of this ratio is one and its deviation influences the achievable calibration accuracy.

2) Measurement Results: A measurement setup was proposed in [28] to evaluate the influence of non-reciprocal transceivers in a realistic environment. By attaching the hardware calibration setup to the MIMO demonstrator, the relative hardware-based calibration (HC) of the base station transceivers can be executed and evaluated. The calibration setup was verified using a network analyzer and the mean value of the ratio $\widetilde{S}_{21,k}/\widetilde{S}_{12,k}$ was computed to be equal to $\widetilde{S}_{21,k}/\widetilde{S}_{12,k} \approx 1.0433 - \mathrm{j}\,0.0466$ within the ISM-band at 2.4 GHz. The value of this ratio results in an error magnitude of approximately -24 dB. To determine the calibration parameter $c_{2,k}$, 1000 measurements were taken regarding (19) and the variance of $c_{2,k}$ versus subcarrier k stays below -22 dB. Fig. 5 shows the mean value of the measured transfer functions with respect to each subcarrier k of the demonstrator transceivers. Fig. 6 depicts the measurement results determined exploiting the multiple antenna demonstrator operating in a multiuser scenario with applied

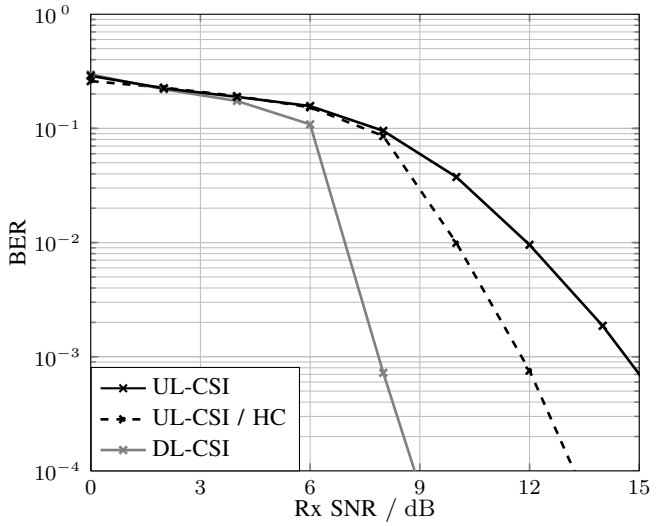

Fig. 6. Measured bit error rates (BER) vs. received signal-to-noise ratio (Rx SNR) of an adaptive multi-user MISO-OFDM system using the MIMO demonstrator for a quasi-static 2×2 multi-user laboratory scenario and different degrees of CSI with applied channel coding.

channel coding. At a BER of 10^{-3}, the hardware-based calibration outperforms the non-calibrated base station (UL-CSI) by approximately 2.7 dB but it is inferior to the DL-CSI-based transmission by approximately 4 dB. This gap motivates a further investigation in terms of a signal-processing-based calibration approach proposed in the following section. One reason for the remaining gap is the temperature dependency observed with respect to the calibration parameters. Although the calibration setup enables an online calibration, this could not be accomplished in our setup due to the inability of simultaneously running one transceiver in transmit mode and the other transceiver in receive mode. Furthermore, it is possible that the assumption of negligible antenna coupling does not hold. In contrast to the presented approach, the additional hardware is avoided in [30] making use of a low-power signal exchange between the different antennas. The advantage of this method is that the load impedance seen by the transceivers remains the same regarding calibration and data transmission phase. This can in general not be ensured when using additional hardware components. Although this may lead to an improved performance in terms of the BER, both hardware-based calibration setups are not able to cope with the coupling effects which underlines the pursuit of a signal-processing-based calibration approach.

IV. Software-Based Downlink Channel Calibration

The system model is established in Section II-B and the corresponding system equations with respect to the downlink channel matrix $\mathbf{H}_k$ as well as the transposed uplink channel matrix $\mathbf{G}_k$ are derived. The hardware-based calibration presented in Section III is only capable of compensating the effect of different gains of the base station transceivers. To be able to compensate for the coupling between the transceiver branches at the base station and to also include the hardware imperfections of the mobile stations into the calibration process, a relation between $\mathbf{H}_k$ and $\mathbf{G}_k$ needs to be established that can be solved with the help of signal processing techniques.

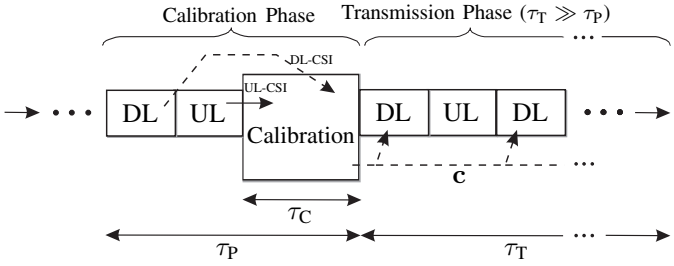

Fig. 7. General workflow of relative calibration procedure.

Once this relation is set up, both $\mathbf{H}_k$ and $\mathbf{G}_k$ have to be made accessible to the base station. In other words, a calibration phase according to Fig. 7 needs to be inserted between regular transmission phases. During the calibration phase, the instantaneous channel state information of the downlink $\mathbf{H}_k$ has to be fed back by the mobile stations to the base station. To build the aforementioned relation between $\mathbf{H}_k$ and $\mathbf{G}_k$, the expression for the transposed uplink matrix $\mathbf{G}_k$ established in (11) is solved for $\mathbf{S}_{\mathcal{MB},k}$ and the result is inserted into the expression for the downlink matrix $\mathbf{H}_k$ given by (10) leading to the following equations

$$\mathbf{H}_k = \mathbf{C}_{\mathcal{M},k} \cdot \mathbf{G}_k \cdot \mathbf{C}_{\mathcal{B},k} \tag{21}$$

$$\mathbf{C}_{\mathcal{M},k} = \mathbf{A}_{\mathrm{R}\mathcal{M},k} \mathbf{W}_{\mathrm{R}\mathcal{M}} \mathbf{W}_{\mathrm{T}\mathcal{M}}^{-T} \mathbf{A}_{\mathrm{T}\mathcal{M},k}^{-1} \tag{22}$$

$$\mathbf{C}_{\mathcal{B},k} = \mathbf{A}_{\mathrm{R}\mathcal{B},k}^{-1} \mathbf{W}_{\mathrm{R}\mathcal{B}}^{-T} \mathbf{W}_{\mathrm{T}\mathcal{B}} \mathbf{A}_{\mathrm{T}\mathcal{B},k} \,. \tag{23}$$

The matrices $\mathbf{C}_{\mathcal{M},k}$ and $\mathbf{C}_{\mathcal{B},k}$ are in general full matrices because they include the mutual coupling effects due to closely spaced antennas. Once these matrices are known it is feasible to exploit the uplink channel state information initially based on the physical reciprocity theorem to adapt to the downlink channel. The calibration vector $\mathbf{c}$ in Fig. 7 consists of the matrix entries of $\mathbf{C}_{\mathcal{M},k}$ and $\mathbf{C}_{\mathcal{B},k}$ and is applied to the transmitted data of the base station to mitigate the hardware effects. The following section introduces the rearranged relation of (21) to make the so-called total least squares (TLS) principles applicable and discusses different methods to solve this specific TLS problem. Section IV-B covers the implementation aspects when running the calibration process on a fixed-point system, e.g., an FPGA.

A. Total Least Squares Principles for Frequency-Domain Calibration

The goal is to obtain a set of linear equations that can be utilized to obtain a solution to the calibration matrices $\mathbf{C}_{\mathcal{M},k}$ and $\mathbf{C}_{\mathcal{B},k}$. Here, the total least squares principle is exploited. Starting with the rearrangement of (21), the following equation is obtained

$$\mathbf{H}_k \mathbf{C}_{\mathcal{B},k}^{-1} - \mathbf{C}_{\mathcal{M},k} \mathbf{G}_k = \mathbf{0}_{N_{\mathcal{M}} \times N_{\mathcal{B}}} \,. \tag{24}$$

Applying the vec-operator to (24) and making use of the identity $\mathrm{vec}\{\mathbf{M} \cdot \mathbf{X} \cdot \mathbf{N}\} = \left(\mathbf{N}^T \otimes \mathbf{M}\right) \cdot \mathrm{vec}\{\mathbf{X}\}$ leads to

$$\left(\mathbf{I}_{N_{\mathcal{B}}} \otimes \mathbf{H}_k\right) \mathrm{vec}\left\{\mathbf{C}_{\mathcal{B},k}^{-1}\right\} - \left(\mathbf{G}_k^T \otimes \mathbf{I}_{N_{\mathcal{M}}}\right) \mathrm{vec}\{\mathbf{C}_{\mathcal{M},k}\} = \mathbf{0}_{N_{\mathcal{M}} N_{\mathcal{B}} \times 1} \tag{25a}$$

and augmenting the matrix $\mathbf{I}_{N_\mathcal{B}} \otimes \mathbf{H}_k$ with the matrix $-\mathbf{G}_k^T \otimes \mathbf{I}_{N_\mathcal{M}}$ yields

$$\underbrace{\left[\mathbf{I}_{N_\mathcal{B}} \otimes \mathbf{H}_k \,,\, -\mathbf{G}_k^T \otimes \mathbf{I}_{N_\mathcal{M}}\right]}_{\triangleq \mathbf{E}_k} \cdot \underbrace{\begin{bmatrix} \mathrm{vec}\left\{\mathbf{C}_{\mathcal{B},k}^{-1}\right\} \\ \mathrm{vec}\left\{\mathbf{C}_{\mathcal{M},k}\right\} \end{bmatrix}}_{\triangleq \mathbf{c}_k} = \mathbf{0}_{N_\mathcal{M} N_\mathcal{B} \times 1} \,, \tag{25b}$$

where the matrix $\mathbf{E}_k \in \mathbb{C}^{N_\mathcal{M} N_\mathcal{B} \times \left(N_\mathcal{M}^2 + N_\mathcal{B}^2\right)}$ and the vector $\mathbf{c}_k \in \mathbb{C}^{\left(N_\mathcal{M}^2 + N_\mathcal{B}^2\right) \times 1}$ have been defined. Literally, a calibration vector $\mathbf{c}_k$ has to be determined for every single subcarrier. Since it is reasonable to assume the baseband-to-baseband behavior of the transceivers by allpass-like transfer functions, the determination of one calibration vector $\mathbf{c}$ regarding the N_sc subcarriers is justified enduring only a small error (cf. Fig. 5). After acquiring the channel state information of several subcarriers K, it is possible to include the additional information by forming the matrix $\mathbf{E} = \left[\mathbf{E}_1^T, \ldots, \mathbf{E}_K^T\right]^T$ with $\mathbf{E} \in \mathbb{C}^{K N_\mathcal{M} N_\mathcal{B} \times \left(N_\mathcal{M}^2 + N_\mathcal{B}^2\right)}$. With the consideration of $K \leq N_\mathrm{sc}$ subcarriers and using (25b), the linear system of equations can be written as

$$\mathbf{E} \cdot \mathbf{c} = \mathbf{0}_{K N_\mathcal{M} N_\mathcal{B} \times 1} \,. \tag{26}$$

Obviously, matrix $\mathbf{E}$ depends on estimates of $\mathbf{G}_k$ and $\mathbf{H}_k$ (cf. [8]). Here, K defines the number of subcarriers used for calibration, where the subcarriers can be arbitrarily chosen due to the frequency-flat transfer functions of the transceivers. To be able to obtain a solution for (26), the number of subcarriers K has to be larger than $K > N_\mathcal{M}/N_\mathcal{B} + N_\mathcal{B}/N_\mathcal{M}$.

Due to the inherent estimation errors in the observation matrix $\mathbf{E}$, the solution for the overdetermined set of equations (26) can be obtained by solving a total least squares optimization problem [8] given by (27).

$$\underset{\Delta\mathbf{E}}{\text{minimize}} \quad \|\Delta\mathbf{E}\|_F \tag{27a}$$

$$\text{such that} \quad (\mathbf{E} + \Delta\mathbf{E})\,\mathbf{c} \approx \mathbf{0}_{K N_\mathcal{B} N_\mathcal{M} \times 1} \,. \tag{27b}$$

The goal is to find a perturbation matrix $\Delta\mathbf{E}$ depending on $\mathbf{E}$ with minimum Frobenius norm that lowers the rank of $\mathbf{E} + \Delta\mathbf{E}$ such that a solution to (27b) can be computed. The matrix $\Delta\mathbf{E}$ is called TLS correction of the optimization problem. Consequently, the solution to (27), the calibration vector $\mathbf{c}$, lies in the right null space of $\mathbf{E}$ and can be computed with the singular value decomposition of $\mathbf{E}$ as shown in [31], [32]. Furthermore, it was proven in [31], [32] that the SVD gives the maximum-likelihood (ML) solution to problem (27). Then, if $\mathbf{E} = \mathbf{U}\mathbf{\Sigma}\mathbf{V}^H$ depicts the SVD and matrix $\mathbf{V} = \left[\mathbf{v}_1, \ldots, \mathbf{v}_{N_\mathcal{B}^2 + N_\mathcal{M}^2}\right]$ denotes the right singular vector space, the estimated solution depends on the rightmost singular vector corresponding to the smallest singular value in $\mathbf{\Sigma}$ such that

$$\mathbf{c} = \mathbf{v}_{N_\mathcal{B}^2 + N_\mathcal{M}^2} \,. \tag{28}$$

Thus, the vector $\mathbf{c}$ in (26) can be fully determined (up to a scalar coefficient, which vanishes due to the reciprocal multiplication in (21)) [8], [33]. With (28) the UL matrices $\mathbf{G}_k$ can be adjusted according to (21) and are used afterwards for the calculation of the pre-equalization filters.

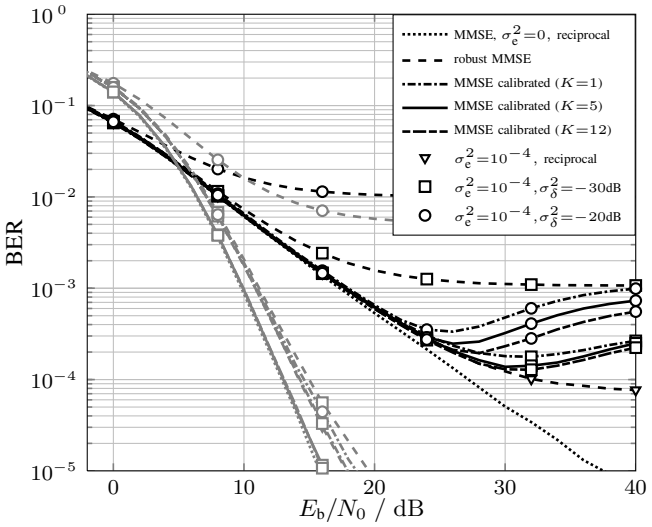

Fig. 8. BER versus E_b/N_0 for an uncoupled system with MMSE pre-equalization and different reciprocity conditions (with (gray-colored) and without (black-colored) applied channel coding).

1) Simulation Results for Uncoupled Systems: In case of a system with negligible mutual coupling, the coupling matrices $\mathbf{W}_{\mathrm{T}\mathcal{B},k}$ and $\mathbf{W}_{\mathrm{R}\mathcal{M},k}$ in (9) are strictly weighted diagonal matrices, resulting in diagonal matrices $\mathbf{C}_\mathcal{B}$ and $\mathbf{C}_\mathcal{M}$ in (21). As a consequence, the optimization problem simplifies as the number of unknowns in (26) reduces to $N_\mathcal{M} + N_\mathcal{B}$. This consequently changes the structure and reduces the size of the matrix $\mathbf{E}$ and the calibration vector $\mathbf{c}$. Multiple measurements are not necessary to obtain a solution if $N_\mathcal{M} > 1$ and $N_\mathcal{B} > 1$. Nevertheless, still further overdetermining this set of equations by incorporating more measurements ($K > 1$) achieves more accurate results [34].

Fig. 8 presents BER results versus E_b/N_0 for linear MMSE pre-equalization. The channel estimation error is set to $\sigma_\mathrm{e}^2 = 10^{-4}$. For completeness, it has to be mentioned that the SNR loss due to the GI is also considered in the results. To ensure a minor complexity for the applied calibration at the BS, only up to twelve subcarriers ($K \in \{1, 5, 12\}$) are used in the calibration process. It can be seen that with occurring reciprocity mismatches the calibrated ordinary MMSE solution clearly outperforms a robust pre-equalizer (see [35], [36]) in terms of uncoded transmission (*solid lines*). The increasing error rates at high signal-to-noise ratios originate from a filter mismatch term due to the imperfect CSI with constant σ_e^2. Furthermore, this interference term is inversely proportional to the noise σ_n^2 [26]. The error rates can be slightly improved by increasing the number of subcarriers K used for the calibration. The coded results instead (*dashed lines*) show that with either using a robust approach or applying calibration excellent results can be obtained as long as the reciprocity mismatch remains smaller or equal to $\sigma_\delta^2 = -30\,\mathrm{dB}$. In this case, almost the performance of a MMSE pre-equalizer with perfect reciprocity and without estimation errors can be achieved. If the reciprocity mismatch is increased to $-20\,\mathrm{dB}$, the robust MMSE pre-equalizer shows severe degradations and only calibration can deal with such a high reciprocity mismatch. This result underlines the need for calibration

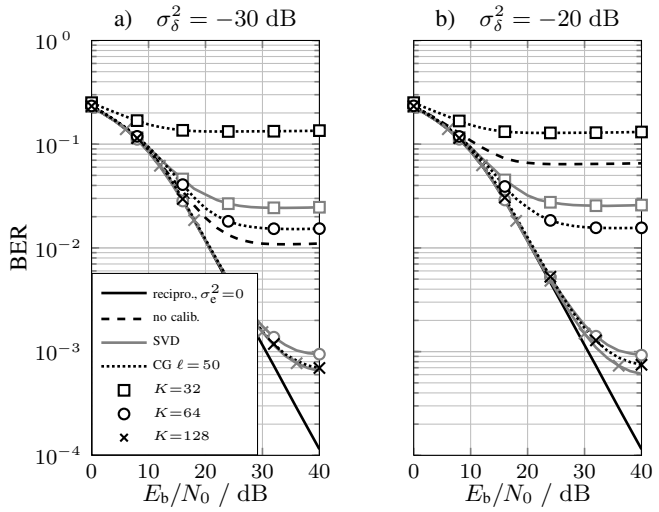

Fig. 9. BER versus E_b/N_0 with BS antenna coupling and variance of the transceiver reflection coefficient of $\sigma_\kappa^2 = -30$ dB and without applied channel coding. The channel estimation error variance is $\sigma_e^2 = 10^{-4}$.

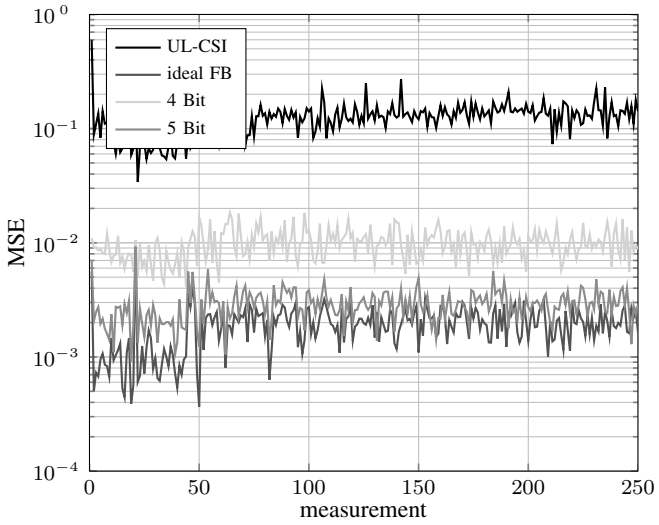

Fig. 10. MSE measurements with 2×2 MIMO demonstrator system in Line-of-Sight scenario assuming uncoupled antenna elements in the calibration algorithm [28].

procedures.

2) Simulation Results for Systems with BS Coupling: Increasing the number of subcarriers K or the number of antennas (or both) makes the exploitation of the SVD to solve the TLS problem (27) computationally prohibitive. In [21], a low-complexity implementation for coupled systems due to the necessary large-scale problem for an increased number of parameters was presented to approximate the SVD. It was shown that the constrained minimization problem in (27) is equivalent to minimizing the so-called Rayleigh quotient

$$f(\mathbf{c}) = \frac{\mathbf{c}^H \mathbf{E}^H \mathbf{E} \mathbf{c}}{\mathbf{c}^H \mathbf{c}}. \tag{29}$$

The minimization of the Rayleigh quotient in turn is equivalent in finding the eigenvector $\mathbf{c}$ associated with the smallest eigenvalue of matrix $\mathbf{E}^H\mathbf{E}$ such that $\min\left\{\|\Delta\mathbf{E}\|_F^2\right\} = \min\{f(\mathbf{c})\}$ equals the minimum singular value and the TLS solution is obtained. An advantage of the Rayleigh quotient is the fact that (29) can be minimized iteratively. One possibility is to use an inverse power method to find the corresponding eigenvector [31]. To avoid the matrix inverse in the inverse power method, this procedure can be efficiently solved via a conjugate gradient (CG) method [21]. Accordingly, Fig. 9 compares the BER results for uncoded systems applying MMSE pre-equalization for different numbers of subcarriers $K \in \{32, 64, 128\}$ exploited during the calibration process and different reciprocity mismatches $\sigma_\delta^2 \in \{-30\,\text{dB}, -20\,\text{dB}\}$. The variance of the reflection coefficients at the BS is fixed to $\sigma_\kappa^2 = -30$ dB for these simulations. The calibration with the considered mutually coupled BS array is carried out with the CG method applying $\ell = 50$ iterations. If the stopping criterion given by a marginally small update of the Rayleigh quotient is reached, the algorithm stops earlier. The results in Fig. 9 a) and b) show a significantly decreased error performance if no calibration is applied. The calibration results for $K = 32$ worsen the performance in terms of the BER compared to the uncalibrated case. Additionally, the results in case of applied calibration are almost independent of the reciprocity mismatch. It can be concluded that only with a large number of calibration carriers, sufficient linear equations are available to ensure a good estimate of the calibration vector $\mathbf{c}$. While the SVD solution achieves a good performance for $K = 64$, the CG method needs more carriers to significantly improve the average BER at the mobile stations. In case of $K = 128$ the CG method has the same performance gain compared to the direct SVD but with considerably reduced complexity. This substantiates the fact that the CG method is especially applicable for large-scale matrix problems.

Overall, the presented frequency-domain-based calibration is able to match the downlink channel with the uplink sufficiently well so that the adaptation to the downlink becomes feasible when exploiting the reciprocity theorem. In contrast, a time-domain-based calibration presented in [37] is not capable of achieving similarly good results. The former can be represented by a structured total least squares problem that is not well suited for OFDM systems due to its complexity and numerical instabilities in certain scenarios.

On the other hand, the high amount of DL channel feedback in UL direction in the calibration phase still renders the application in high-rate adaptive communication systems difficult. Nevertheless, in [38], a recursive implementation of the TLS principles containing an additional QR decomposition (QRD) was presented in combination with directly quantized feedback that is distributed over the OFDM time-frequency grid. Interpolation between calibration carriers results in the reduction of feedback necessary in frequency direction [39] while efficiently updating the $\mathbf{R}$ matrix of the QRD can help tracking the varying parameters in time [38].

Regarding an evaluation of the calibration scheme in a practical system, the MIMO demonstrator is used and uncoupled antenna elements are assumed throughout the measurements. This assumption leads to the reduced TLS problem with $N_\mathcal{M} + N_\mathcal{B}$ unknown coefficients. Hence, Fig. 10 shows the mean square error (MSE) results between the true measured DL channel, the measured UL and the calibrated UL channel,

respectively. In case of the uncalibrated MIMO demonstrator, the MSE remains at around 10% in each duplex phase, whereas the possible MSE reduction is from 10% to 0.2% on average for ideal (analog) feedback. With quantized feedback, assuming five bits per real coefficient per DL channel, the MSE performance shows comparably good results. The implementation of only four bit feedback per real coefficient leads to MSE results around one order of magnitude larger than in case of perfect feedback. Consequently, the amount of feedback must be large enough. To reduce the feedback, the data to be fed back can be split up into multiple packets or (in terms of multicarrier systems) into several OFDM symbols and distributed over multiple subcarriers.

B. Hardware Implementation Aspects

The investigation of the presented algorithms based on TLS principles indicated that the accuracy of the calibration is of great importance at the expense of meeting any latency constraints. Therefore, this section introduces efficient accurate low-complexity calculations suitable for real-time implementations. Finally, a calibration module is implemented on an FPGA and first measurement results show excellent performance in terms of accuracy and FPGA area consumption. As FPGAs already execute many digital signal processing functions/algorithms in the BS, the calibration can potentially be embedded in one of the existing FPGAs. An advantage of FPGAs towards very-large-scale integration circuits (VLSI) is the possibility of an easy reconfiguration and lower costs with respect to small-scale production. In addition, FPGAs have better timing behavior compared to Digital Signal Processors (DSPs).

1) Low-Complexity TLS Calibration: The implementation of the low-complexity TLS calibration on an FPGA is achieved regarding an uncoupled system, i.e., $\mathbf{C}_{\mathcal{B}}$ and $\mathbf{C}_{\mathcal{M}}$ are diagonal matrices. According to Section IV-A the optimization problem of (27) can be solved by the application of the SVD. In order to achieve a reduction in complexity an efficient approximation to the SVD is obtained. The latter can be accomplished by several existing algorithms [31], [32], in particular by the rank-revealing ULV and URV decomposition [40], where U and V are acronyms for a unitary, R for a right and L for a left matrix. Here, the ULV decomposition (ULVD) represents the matrix $\mathbf{E}$ by

$$\mathbf{E} = \mathbf{U}'\mathbf{L}\mathbf{V}'^{H} \tag{30}$$

where the unitary matrices $\mathbf{U}'$ and $\mathbf{V}'$ are approximations of $\mathbf{U}$ and $\mathbf{V}$ of a SVD on $\mathbf{E}$. $\mathbf{L}$ is a lower triangular matrix, which has the same singular values as $\mathbf{E}$. This ULVD will be achieved by two QR decompositions. The first QRD obtains $\mathbf{QR} = \mathbf{E}$, then the second QRD is applied on the conjugate transpose of $\mathbf{R}$ such that

$$\mathbf{E} = \mathbf{Q}\begin{pmatrix}\mathbf{R}_0\\ \mathbf{0}\end{pmatrix} = \mathbf{Q}\tilde{\mathbf{R}}^{H}\tilde{\mathbf{Q}}^{H} \tag{31a}$$

$$\text{with}\quad \mathbf{R}_0^{H} = \tilde{\mathbf{Q}}\tilde{\mathbf{R}} \tag{31b}$$

where $\mathbf{Q} \triangleq \mathbf{U}'$, $\tilde{\mathbf{Q}} \triangleq \mathbf{V}'$ and $\tilde{\mathbf{R}}^{H} \triangleq \mathbf{L}$. Finally, the rightmost column of $\tilde{\mathbf{Q}}$ contains an approximation of the TLS solution vector $\mathbf{c}$ as in (28). The computational complexity is reduced by the fact that the second QRD in (31b) is only performed on $\mathbf{R}_0^{H} \in \mathbb{C}^{N_{\mathcal{B}}+N_{\mathcal{M}}\times N_{\mathcal{B}}+N_{\mathcal{M}}}$, so that the dimension of $\mathbf{R}_0$ depends solely on the number of BS antennas $N_{\mathcal{B}}$ and the number of users $N_{\mathcal{M}}$. Furthermore, the computational complexity is significantly reduced by omitting the calculation of the orthogonal matrix $\mathbf{Q}$ in the first QRD.

In order to compute the QRDs in (31a) some considerations for a suitable hardware implementation have to be made. Especially three methods have been established to compute the QRD: the Householder transformations, the Gram-Schmidt process and Givens rotations (sometimes also called Jacobi rotations). Concerning an FPGA implementation, the Householder transformation has the disadvantage that it cannot be parallelized. The Gram-Schmidt algorithm is numerically unstable. Furthermore, the Gram-Schmidt process requires square-root operations sharing this necessity with the numerically more stable modified Gram-Schmidt [31]. On the other hand, the Givens rotation allows a parallel computational structure and with the well-known CORDIC (COordinate Rotation DIgital Computer) algorithm [41] costly divisions or square root computations can be avoided in the Givens rotation. Another advantage of the CORDIC based Givens rotation used in this work is that the QRD can be adaptively implemented in hardware. If this is considered in the design, the QRD can be used for several numbers of calibration carriers K. In this way, an adaptive calibration is possible. Because the number of columns of $\mathbf{E}$ is independent of K, the Givens rotations can be parallelized for a fixed number of columns. If K is incremented, only the computation time is rising slightly because further rotations are executed on the additional rows of matrix $\mathbf{E}$ in the first QRD. The computation time of the second QRD is not affected by changing K.

2) FPGA Implementation: As mentioned before, the CORDIC algorithm is a well-known iterative method to calculate trigonometric and algebraic functions like sine, cosine, square root or division [41], [42]. The principle of CORDIC is based on m serial micro-rotations. As CORDIC only uses bitshifting, addition and subtraction operations, it is particularly suitable for hardware implementation of complex algorithms. The disadvantage of an increasing latency for iterative algorithms is reduced by a pipelined implementation. As a consequence of the iterative topology of the CORDIC algorithm, the numerical accuracy depends on the number of micro-rotations. Furthermore, the accuracy is reduced by the conversion from floating-point to fixed-point, which is necessary for efficient hardware realization. A quantization scheme that ensures a solution very close to that obtained by floating-point operations is acquired by simulations. Regarding floating-point results, an optimal quantization is achieved by using 16 bit word-length with 12 fractional bits. Fig. 11 shows the dependency of the BER on the number of micro-rotations m with linear MMSE pre-equalization. The channel estimation error variance is again set to $\sigma_{\mathrm{e}}^2 = 10^{-4}$ and the reciprocity error variance is $\sigma_{\delta}^2 = -20$ dB. The calibration is simulated with an equivalent fixed-point FPGA-model. For more than $m = 11$ micro-rotations, no improvement can be achieved in the uncoded case, while for the coded transmission $m = 8$ micro-rotations are sufficient to obtain the best performance.

An interesting effect can be observed by the error prop-

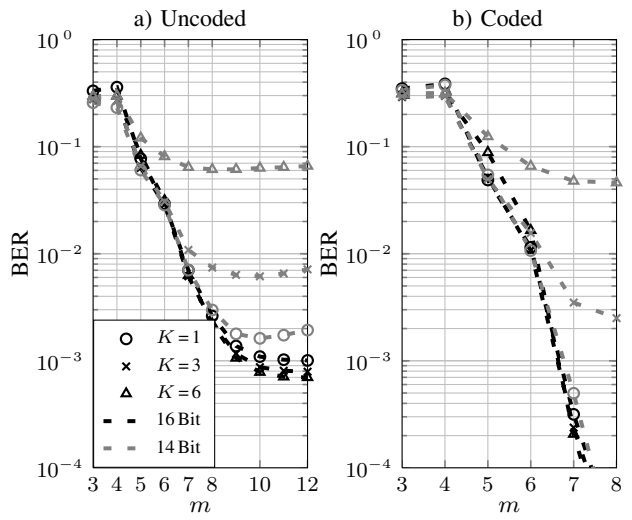

Fig. 11. BER at $E_b/N_0 = 40$ dB for an uncoupled MU-MISO-OFDM system versus different numbers of micro-rotations m in the CORDIC; channel estimation error variance set to $\sigma_e^2 = 10^{-4}$, $\sigma_\delta^2 = -20$ dB, a) without, b) with applied channel coding.

agation in the ULVD in case of a smaller number of bits used for quantization and larger K. As Fig. 11 shows the best performance for 14 bit quantization is achieved by $K = 1$, an increase of K does not induce a better performance such as for 16 bit quantization. Instead, the performance is getting worse. The increasing BER for the 14 bit quantization at $m > 10$ in Fig. 11 a) originates from the circumstance that for this scenario 10 fractional bits are used and for $m > 10$ the fixed-point data will be shifted for $m > 10$ positions to the right within the CORDIC. In this case the rounding error is increasing because m is greater than the fraction length of the fixed-point data. This behavior has to be considered if the calibration is realized for coupled antennas, where $K \gg 1$ calibration carriers are needed. In this case, a longer word length or a more precise rounding is required.

As shown, the number of micro-rotations has a significant impact on the accuracy of the calibrated UL channel. For a sufficient calibration performance $m = 8$ micro-rotations are required in the coded case. In order to enhance the throughput the CORDIC and the QRD can be parallelized and pipelined. To get a trade-off of precision, computing time and hardware usage a 2nd-order unrolled CORDIC-unit is applied [43]. The order of the CORDIC architecture denotes the number of micro-rotations in one clock cycle. Concerning the 2nd-order architecture, four 2nd-order CORDIC units perform one Givens-rotation in four clock cycles with $m = 8$ micro-rotations. If a higher order of the CORDIC is used, the combinatorial path is getting longer and the maximum frequency f_{clk} of the circuit is reduced.

3) Implementation Results: The ULVD has been implemented in a calibration module for a 2×2 MU-MISO-System on a Xilinx Virtex 5 FPGA (XC5VSX50T) [44]. To benefit from the fact that more channel measurements improve the calibration performance, we decided to design an adaptive calibration where the number of calibration carriers can be changed from $K = 1$ to $K = 6$ in single steps. Therefore, also the latency caused by the calibration can be adjusted from

TABLE II
SYNTHESES RESULTS FOR THE XILINX VIRTEX 5 FPGA (XC5VSX50T).

	adaptive		fix $K = 1$	
	total	%	total	%
Slices	24 739	97	16 842	66
LUT	40 417	79	31 965	63
FF	17 076	33	7 785	15
Multiplier	34	26	34	26
maximum f_{clk}	108.5 MHz		129.2 MHz	
t_{TLS}/K	2.61 µs		2.09 µs	

15.66 µs to 2.61 µs. In addition, this short calculation time allows quick updates in a recursive implementation of the TLS with iterative feedback using a QR-based algorithm described in [38]. This reduces the amount of reserved bits for calibration in the UL transmission. The adaptive ULVD implementation can decompose matrices up to a size of $\mathbb{C}^{24\times4}$. In order to compare the device utilization and the calculation time, a second design is synthesized, where K is fixed to one, which implies that only the matrix $\mathbf{E} \in \mathbb{C}^{4\times4}$ can be decomposed. According to Fig. 11, a quantization of 16 bit word length with 12 fractional bits is chosen. Table II shows the usage of slices, lookup-tables (LUT), flip-flops (FF) and multipliers. Furthermore, the percental utilization of the available hardware of the FPGA after syntheses is given. Additionally, the maximum clock frequency f_{clk} and the computation time of the TLS solution per calibration carrier t_{TLS}/K at maximum f_{clk} are listed. In consequence of the increased control complexity for the adaptive module the calibration time per subcarrier raises. In order to evaluate the computational reduction by using the ULVD instead of a SVD the calculation time is compared to the work given in [45]. There, a complex-valued 4×4 SVD unit for 180 nm CMOS technology is given and with 8 CORDIC micro-rotations the SVD takes 10.75 µs at a clock frequency of 272 MHz. In this work, the TLS solution is calculated out of a 4×4 calibration-matrix in 2.09 µs at a clock frequency of 129 MHz. However, both implementations use completely different technologies so that a fair comparison is not possible, especially for the power consumption and area or device utilization, respectively. But it shows that the ULVD is a promising approach to obtain the TLS solution with less effort compared to the SVD.

V. CONCLUSION AND FUTURE WORK

The application of calibration methods has been studied for multi-user MISO-OFDM systems utilizing time-division duplex. The latter additionally exploit joint pre-processing at the base station. The successfully applied calibration methods enable the utilization of the uplink channel estimate due to the reciprocity theorem. With low-cost transceiver solutions the direct utilization of the baseband uplink channel estimate for downlink adaptation is impossible due to the non-reciprocal properties of the transceivers. Additional hardware-based circuitries ensuring an online calibration capability show improvements in terms of BER performance in measurements while significant receive SNR losses still remain due to the inability of accounting for antenna coupling. The signal-processing-based relative calibration is able to compensate for

these effects almost perfectly when using the channel estimates on every other subcarrier during the calibration process. Unfortunately, the approach of a software-based relative calibration requires a special calibration phase degrading the total system throughput. Exploiting the suggested recursive implementation of the calibration algorithm mitigates this degradation efficiently. To bridge the gap between signal processing and hardware implementation, the effect of a quantized feedback was also investigated based on a MIMO demonstrator. In this case, 5 bits per real-valued channel coefficient lead to almost identical results when comparing to the ideally fed back channel state information. Furthermore, initial aspects of the computation of the needed total least squares solution on an FPGA is studied. The theoretical background provides insight in low-complexity solutions based on the CORDIC algorithm, which can be applied to solve the required matrix decompositions. In the future, the considerable improvements using signal processing calibration will be further investigated on off-the-shelf hardware MIMO solutions [28], [46], especially the implementation of the recursive algorithm on an FPGA will be pursued.

REFERENCES

[1] G. S. Smith, "A direct derivation of a single-antenna reciprocity relation for the time domain," *IEEE Trans. Antennas Propag.*, vol. 52, no. 6, pp. 1568–1577, Jun. 2004.

[2] T. C. W. Schenk, *RF Imperfections in High-Rate Wireless Systems: Impact and Digital Compensation*. Springer, 2008.

[3] F. Horlin and A. Bourdoux, *Digital Compensation for Analog Front-Ends - A New Approach to Wireless Transceiver Design*. John Wiley & Sons, 2008.

[4] V. Jungnickel, U. Kruger, G. Istoc, T. Haustein, and C. von Helmolt, "A MIMO system with reciprocal transceivers for the time-division duplex mode," in *Proc. 2004 IEEE Antennas and Propagation Society Intern. Symp.*, vol. 2, pp. 1267–1270.

[5] A. Bourdoux, B. Come, and N. Khaled, "Non-reciprocal transceivers in OFDM/SDMA systems: impact and mitigation," in *Proc. 2003 IEEE Radio and Wireless Conference*, pp. 183–186.

[6] J. Liu, G. Vandersteen, J. Craninckx, M. Libois, M. Wouters, and F. Petré, "A novel and low-cost analog front-end mismatch calibration scheme for MIMO-OFDM WLANs," in *Proc. 2006 IEEE Radio and Wireless Symposium*, pp. 219–222.

[7] G. Fettweis, M. Löhning, D. Petrovic, M. Windisch, P. Zillmann, and W. Rave, "Dirty RF: a new paradigm," in *Proc. 2005 IEEE Intern. Symp. On Personal, Indoor And Mobile Radio Comm.*

[8] M. Guillaud, "Transmission and channel modeling techniques for multiple-antenna communication systems," Ph.D. thesis, Ecole Nationale Superieure des Telecomm., Paris, France, Jul. 2005.

[9] M. Guillaud, D. T. M. Slock, and R. Knopp, "A practical method for wireless channel reciprocity exploitation through relative calibration," in *2005 Intern. Symp. on Signal Processing and its Applications*.

[10] F. Kaltenberger and M. Guillaud, "Exploitation of reciprocity in measured MIMO channels," in *COST 2100, 9th Management Committee Meeting, TD(09)950*, Vienna, Austria, Sep. 2009.

[11] F. Kaltenberger, H. Jiang, M. Guillaud, and R. Knopp, "Relative channel reciprocity calibration in MIMO/TDD systems," in *Proc. 2010 Future Network and Mobile Summit*.

[12] P. Xia, S. Zhou, and G. B. Giannakis, "Adaptive MIMO OFDM based on partial channel state information," *IEEE Trans. Signal Process.*, vol. 52, no. 1, pp. 202–213, Jan. 2004.

[13] W. Keusgen and B. Rembold, "Konzepte zur realisierung von MIMO-frontends," *Frequenz - Zeitschrift für Telekomm.*, vol. 55, no. 11-12, pp. 301–309, Nov. 2001.

[14] W. Keusgen, "Antennenkonfiguration und kalibrierungskonzepte für die realisierung reziproker mehrantennensysteme," Ph.D. thesis (in German), RWTH Aachen, Germany, Oct. 2005.

[15] C. A. Balanis, *Antenna Theory - Analysis and Design*, 3rd ed. John Wiley & Sons, 2005.

[16] H. Yordanov, M. T. Ivrlač, P. Russer, and J. A. Nossek, "Arrays of isotropic radiators—a field-theoretic justification," in *2009 Intern. ITG Workshop on Smart Antennas*.

[17] M. T. Ivrlač and J. A. Nossek, "Toward a circuit theory of communication," *IEEE Trans. Circuits and Systems I: Regular Papers*, vol. 57, no. 7, pp. 1663–1683, Jul. 2010.

[18] T. Svantesson, "The effects of mutual coupling using a linear array of thin dipoles of finite length," in *1998 IEEE Signal Processing Workshop on Statistical Signal Processing*.

[19] D. Pozar, *Microwave Engineering*, 2nd ed. John Wiley & Sons, 1998.

[20] 3GPP, "TS 36.300 Evolved Universal Terrestrial Radio Access (E-UTRA) and Evolved Universal Terrestrial Radio Access Network (E-UTRAN); overall description; Stage 2," 3GPP, Mar. 2013.

[21] M. Petermann, M. Stefer, D. Wübben, M. Schneider, and K.-D. Kammeyer, "Low-complexity calibration of mutually coupled non-reciprocal multi-antenna OFDM transceivers," in *2010 Intern. Symp. on Wireless Comm. Systems*.

[22] M. Stefer and M. Schneider, "On modeling antenna coupling for adaptive MIMO-OFDM systems," in *2010 Intern. ITG Workshop on Smart Antennas*.

[23] S. A. Schelkunoff and H. T. Friis, *Antennas — Theory and Practice*, 3rd ed. John Wiley & Sons, 1966.

[24] C. Degen, "Frequency-domain signal processing for space-division multiple access with consideration of front-end imperfections," Ph.D. thesis, RWTH Aachen, Germany, Jul. 2005.

[25] R. Habendorf, "Vorentzerrung für die räumlich überlagerte kommunikation mit verteilten empfängern," Ph.D. thesis (in German), TU Dresden, Germany, Dec. 2008.

[26] M. Petermann, D. Wübben, and K.-D. Kammeyer, "Evaluation of encoded MU-MISO-OFDM systems in TDD mode with non-ideal channel reciprocity," in *2010 Intern. ITG Conference on Source and Channel Coding*.

[27] M. Stefer, M. Petermann, M. Schneider, D. Wübben, and K.-D. Kammeyer, "Enhanced adaptive downlink transmission in MIMO-OFDM systems by hardware-based calibration," in *2011 Intern. OFDM-Workshop*.

[28] ——, "Influence of non-reciprocal transceivers at 2.4 GHz in adaptive MIMO-OFDM systems," in *2009 Intern. OFDM-Workshop*.

[29] J. Rinas, R. Seeger, L. Brötje, S. Vogeler, T. Haase, and K.-D. Kammeyer, "A multiple-antenna system for ISM-band transmission," *EURASIP J. Applied Signal Process.*, vol. 2004, no. 9, pp. 1407–1419, Aug. 2004.

[30] P. Zetterberg, "Experimental investigation of TDD reciprocity-based zero-forcing transmit precoding," *EURASIP J. Adv. Signal Process.*, vol. 2011, pp. 5:1–5:10, Jan. 2011. Available: http://dx.doi.org/10.1155/2011/137541

[31] G. H. Golub and C. F. V. Loan, *Matrix Computations*, 3rd ed. Johns Hopkins University Press, 1996.

[32] S. V. Huffel and J. Vandewalle, *The Total Least Squares Problem: Computational Aspects and Analysis*. Society for Industrial and Applied Mathematics (SIAM), 1991.

[33] G. H. Golub and C. F. V. Loan, "An analysis of the total least squares problem," *SIAM J. Numerical Analysis*, vol. 17, no. 6, pp. 883–893, Dec. 1981.

[34] M. Petermann, D. Wübben, and K. D. Kammeyer, "Calibration of non-reciprocal transceivers for linearly pre-equalized MU-MISO-OFDM systems in TDD mode," in *2009 Intern. OFDM-Workshop*, pp. 53–57.

[35] R. Habendorf and G. Fettweis, "Pre-equalization for TDD systems with imperfect transceiver calibration," in *Proc. 2008 IEEE Vehicular Technology Conference – Spring*.

[36] M. Joham, K. Kusume, M. Gzara, W. Utschick, and J. A. Nossek, "Transmit Wiener filter for the downlink of TDD DS-CDMA systems," in *Proc. 2002 IEEE International Symposium on Spread Spectrum Techniques and Applications*, vol. 1, pp. 9–13.

[37] M. Petermann, D. Wübben, A. Dekorsy, and K.-D. Kammeyer, "Calibration for single-carrier preFDE transceivers based on property mapping principles," in *2011 Intern. ITG Workshop on Smart Antennas*.

[38] M. Petermann, F. Ludwig, D. Wübben, S. Paul, and K.-D. Kammeyer, "Effects of downlink channel quantization on the performance of relative calibration in OFDM systems," in *2011 Intern. OFDM-Workshop*.

[39] Y. Hara, Y. Yano, and H. Kubo, "Antenna array calibration using frequency selection in OFDMA/TDD systems," in *2008 IEEE Global Telecomm. Conference*.

[40] S. V. Huffel and H. Zha, "An efficient total least squares algorithm based on a rank-revealing two-sided orthogonal decomposition," *Numerical Algorithms*, vol. 4, no. 1, pp. 101–133, 1993.

[41] J. E. Volder, "The CORDIC trigonometric computing technique," *IRE Trans. Electron. Computers*, vol. EC-8, no. 3, pp. 330–334, 1959.

[42] B. Parhami, *Computer Arithmetic Algorithms and Hardware Designs*. Oxford University Press, 2000.

[43] S. Wang, V. Piuri, and J. E. E. Swartzlander, "A unified view of CORDIC processor design," in *Proc. 1996 IEEE Midwest Symposium on Circuits and Systems*, vol. 2, pp. 852–855.
[44] Xilinx, Virtex-5 FPGA Data Sheet, 2010. Available: http://www.xilinx.com/support/documentation/data_sheets/ds202.pdf.
[45] C. Studer, P. Blosch, P. Friedli, and A. Burg, "Matrix decomposition architecture for MIMO systems: design and implementation trade-offs," in *Conference Record 2007 Asilomar Conference on Signals, Systems and Computers*, pp. 1986–1990.
[46] Lyrtech, Quad Dual Band RF Transceiver 4-channel, MIMO, RF analog front end, Product Sheet, 2010. Available: http://www.lyrtech.com/products/quad_dual_band_rf_transceiver.php.

Mark Petermann received the Dipl.-Ing. degree in electrical engineering from the University of Bremen, Germany, in 2005. From 2005 to 2012 he was with the Department of Communications Engineering at the University of Bremen, where he received the Dr.-Ing. degree in 2012. Currently, he is with the ATLAS ELEKTRONIK GmbH. His main fields of interest are multi-user MIMO communications, image and correlation processing.

Markus Stefer received the Dipl.-Ing. degree in electrical engineering from the University of Aachen, Germany, in 2007. Currently, he is with the RF & Microwave Engineering Laboratory at the University of Bremen, Germany, where he is also working towards his Ph.D. degree. His main fields of interest are the modeling of RF components for communication systems, signal processing in multiple antenna systems and localization and tracking.

Frank Ludwig received the Dipl.-Ing. degree in electrical engineering from the University of Bremen, Germany, in 2009. Currently, he is with the Institute of Electrodynamics and Microelectronics, University of Bremen, Germany, where he is currently working towards his Ph.D. degree. His focus is on the implementation of digital signal processing algorithms for wireless communications on FPGAs and prototype development for wireless multiantenna LTE systems.

Dirk Wübben (S'02-M'06-SM'12) received the Dipl.-Ing. (FH) degree in electrical engineering from the University of Applied Science Münster, Germany, in 1998, and the Dipl.-Ing. (Uni) degree and the Dr.-Ing. degree in electrical engineering from the University of Bremen, Germany, in 2000 and 2005, respectively. He was a visiting student at the Daimler Benz Research Departments in Palo Alto, California, in 1997, and in Stuttgart, Germany, in 1998. From 1998 to 1999 he was with the Research and Development Center of Nokia Networks, DÃ$\frac{1}{4}$sseldorf, Germany. In 2001, he joined the Department of Communications Engineering, University of Bremen, Germany, where he is currently a senior researcher and lecturer.

Martin Schneider received his Diploma and Doctorate degree in Electrical Engineering and Information Technology from the University of Hannover, Germany, in 1992 and 1997, respectively. From 1997 to 1999, he was with Bosch Telecom GmbH in Backnang, Germany, where he developed microwave components for point-to-point and point-to-multipoint radio link systems. In November 1999, he joined the Corporate Research and Advanced Development division of Robert Bosch GmbH in Hildesheim, Germany. As a project and section manager of the "Wireless Systems" group he focused on research and development of phased array and smart antenna concepts for automotive radar sensors at 24 GHz and 77 GHz. From 2005 to 2006, he was with the business unit Automotive Electronics of Robert Bosch GmbH in Leonberg, Germany. As a section manager he was responsible for the "RF electronics" for automotive radar sensors. Since March 2006, he has been a full professor and head of the RF & Microwave Engineering Laboratory at the University of Bremen, Germany.

Steffen Paul (S'86-M'93) studied electrical engineering at Technical University Dresden and Technical University Munich, Germany, from 1984-1989, where he received his Diploma (Dipl.-Ing.) degree in 1989. From 1989 to 1997 he was working at the Institute of Network Theory and Circuit Design of the same institution. In 1993 he received the Dr.-Ing. degree. He held a postdoctoral position at the EECS department of the University of California, Berkeley in 1994 to 1995. From 1997 to 2007 he was working at Infineon Technologies (former Siemens Semiconductor group) in the areas of memory design, xDSL and UMTS concept engineering. He joined the University Bremen in 2007 as a full professor for electromagnetic theory and microelectronic systems.

Karl-Dirk Kammeyer (M'95) received the Dipl.-Ing. in electrical engineering from Berlin University of Technology, Berlin, Germany, in 1972, and the Ph.D. degree (Dr.-Ing.) from Erlangen University, Erlangen, Germany, in 1977. From 1972 to 1979, he worked in the field of data transmission, digital signal processing, and digital filters at the Universities of Berlin, Saarbrucken, and Erlangen, all in Germany. From 1979 to 1984, he was with Paderborn University, Paderborn, Germany, where he was engaged in the development of digital broadcasting systems. During the following decade, he was a Professor for digital signal processing in communications at Hamburg University of Technology, Hamburg, Germany. In 1995, he was appointed as Professor for telecommunications at the University of Bremen, Bremen, Germany.